

Enhanced Stability Lithium-Ion Battery Based on Optimized Graphene/Si Nanocomposites by Templated Assembly

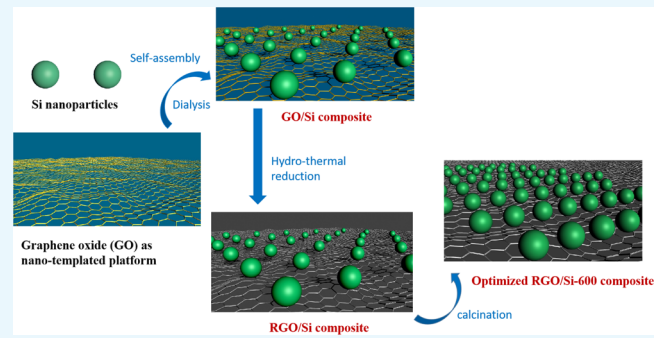
Long Liu,[†] Xinxin Li,^{*,†,§,ID} Guoqing Zhang,[†] Zengyao Zhang,[†] Chenhui Fang,[†] Hong Ma,[†] Wen Luo,^{*,†,§} and Zhongyun Liu[†]

[†]School of Materials and Energy, Guangdong University of Technology, Guangzhou 51006, PR China

[‡]School of Chemical and Biomolecular Engineering, Georgia Institute of Technology, 311 Ferst Dr. NW, Atlanta, Georgia 30332, United States

Supporting Information

ABSTRACT: Considering the sharp increase in energy demand, Si-based composites have shown promise as high-performance anodes for lithium-ion batteries during the last few years. However, a significant volume change of Si during repetitive cycles may cause technical and security problems that limit the particular application. Here, an optimized reduced graphene oxide/silicon (RGO/Si) composite with excellent stability has been fabricated via a facile templated self-assembly strategy. The active silicon nanoparticles were uniformly supported by graphene that can further form a three-dimensional network to buffer the volume change of Si and produce a stable solid-electrolyte interphase film due to the increased specific surface area and enhanced intermolecular interaction, resulting in an increase of electrical conductivity and structural stability. As the anode electrode material of lithium-ion batteries, the optimized 10RGO/Si-600 composite showed a reversible high capacity of 2317 mA h/g with an initial efficiency of 93.2% and a quite high capacity retention of 85% after 100 cycles at 0.1 A/g rate. Especially, it still displayed a specific capacity of 728 mA h/g after 100 cycles at a reasonably high current density of 2 A/g. This study has proposed the optimized method for developing advanced graphene/Si nanocomposites for enhanced cycling stability lithium-ion batteries.



1. INTRODUCTION

The rapid development of lithium-ion batteries (LIB) is driven by a growing energy storage demand of new energy vehicles and portable electronic equipment.^{1–4} To meet the requirements of high-power density and long lifespan for large-scale LIB application, the improvement of energy density and long-term stability for electrode materials is distinctly important. In recent years, silicon has attracted much attention as the most promising substitute to the traditional graphite anode materials owing to the high theoretical capacity of about 4200 mA h/g and low operating potential.^{5,6} However, the large volume expansion and pulverization of silicon during the charge and discharge processes lead to fast capacity fade and damage to the electrode that limit particular LIB applications.⁷

To address the main drawback, scientists have put much effort focus on mitigating capacity fading in Si-based anodes, such as adding novel binders,^{8–11} mixing additives,^{12–14} coating high-conductivity materials,^{15–19} and designing special silicon nanostructures.^{19–22} Besides the above-modified methods, the silicon/nanocarbon composite with diverse structures have been considered as the most potent strategy to improve the performance of silicon material.^{23,24}

Recently, graphene has been utilized to modify silicon-based anode materials for improving the comprehensive electro-

chemical performance, preventing the aggregation of Si particles exposed to the electrolyte, providing skeleton-support for buffering the mechanical stress, and enhancing the lithium-ion transportation capability.^{25,26} Chou et al.²⁷ first prepared Si/graphene composite via a simple manual mixing method in 2010. The results displayed that the anode materials maintained a capacity of 1168 mA h/g and an average Coulombic efficiency of 93% after 30 cycles at 0.1 A/g. Chang et al.²⁸ successfully prepared a silicon/reduced oxide graphene (RGO) nanocomposite with a three-dimensional multilayer structure, exhibiting an excellent reversible capacity up to 2300 mA h/g at 0.05 C (120 mA/g) and 87% capacity retention (up to 630 mA h/g) at 10 C after 152 cycles. Park et al.²⁹ presented that Si nanoparticles could be entrapped RGO nanosheets by simple self-assembly without any chemical/physical linkers. The test results displayed the improved cyclability (1481 mA h/g after 50 cycles) and favorable high-rate capability. Son et al.³⁰ presented multilayer graphene directly grown on the Si nanoparticles surface by the chemical vapor deposition method. The results revealed a significant

Received: July 7, 2019

Accepted: August 26, 2019

Published: October 22, 2019



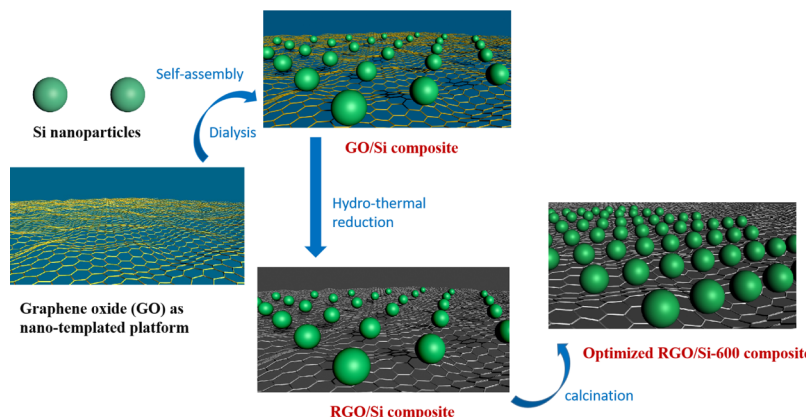


Figure 1. Schematic illustration of the synthetic strategy of the optimized RGO/Si composite.

improvement of the performance. Zhou et al.³¹ fabricated Si/graphene composite film decorated by bovine serum albumin via electrostatic self-assembly, vacuum filtration, and annealing but the electrochemical performance of this electrode is not good enough. Zhang et al.³² proposed 3D porous Si/RGO anode materials with tunable pore size via controllable evaporation. The results revealed that Si/RGO anode after evaporation drying for 3.5 h exhibits a high reversible specific capacity of 1563 mA h/g at 50 mA/g, 90% capacity retention after 100 cycles, and superior rate capability (955 mA h/g at 2 A/g). However, although a large amount of research is focused on the silicon/graphene anode materials, few works focus on exploring an efficient and feasible method for preparing large-scale and stable-structured silicon/graphene anode materials, simultaneously keeping the high reversible capacity and long-term stability at a high rate current.

Here, we report an optimized RGO/Si composite via a scalable and effective method shown in Figure 1. Si nanoparticles with controllable size are uniformly supported by the graphene nanosheets to form a 3D network. The increased specific surface area and enhanced intermolecular interactions at solid-state result in a remarkable increase in specific capacity and cycle stability. This kind of anode material opens a way to the high-stability LIBs.

2. RESULTS AND DISCUSSION

2.1. Structural Characterization. The XRD patterns of P-Si and RGO/Si composites at different conditions are shown in Figure 2. The sharp peaks of P-Si and RGO/Si samples at 28.5°, 38°, 57°, 69.5°, and 76.6° are assigned to (111), (220), (311), (400), and (331) planes of crystalline Si (PDF#05-0565).^{33,34} In addition, RGO exhibited characteristic

peaks at 27° which belong to the (002) plane.³⁵ Obviously, it can be found that the peaks at (002) were enhanced due to the increased content of graphene in the RGO/Si composites compared to the P-Si. It also can be seen that the crystal structure of Si nanoparticles was not destroyed during the self-assembly and hydrothermal process. Moreover, compared to 10RGO/Si, the peaks of silicon in the 10RGO/Si-600 have obviously increased, whereas the carbon peak has no change, indicating that the annealing process further promoted growth of the silicon grains and enhanced the intermolecular interaction between graphene and Si nanoparticles.

The XPS test was carried out to analyze the surface chemical state of the composites and the role of calcination. In the survey spectra of 10RGO/Si and 10RGO/Si-600 (Figure 3a), the elements, O, C, and Si arise from graphene nanosheets and Si nanoparticles, which is different with the P-Si (Figure S1). To further illustrate the role of calcination, we applied the XPS region spectra of C 1s and Si 2p for 10RGO/Si and 10RGO/Si-600. From the C 1s region of the 10RGO/Si-600, there are four peaks (Figure 3b) of 284.4, 285.0, 286.0, and 289.4 eV, which can be assigned to C–Si, C–C, C–O, and C=O bands, respectively. Moreover, from the Si 2p region of the 10RGO/Si-600 (Figure 3c), three evident peaks at 99.8, 101.2, and 103.9 eV could be attributed to the Si–Si, Si–C, and Si–O bands. Compared with the C 1s and Si 2p region of 10RGO/Si, the additional C–Si and Si–C band revealed the formation of chemical bond linkage in RGO/Si nanocomposite.^{36,37} This kind of optimized nanocomposite after calcination is beneficial to improve the electrochemical performance because of the increased specific surface area and enhanced intermolecular interaction.^{38,39} To demonstrate the changes of the specific surface area, the Brunauer–Emmett–Teller (BET) test was applied (Figure S2 and Table S1). It can be found that the specific surface area of the 10RGO/Si (482 m²/g) composite is an order of magnitude higher than the P-Si (30 m²/g). Furthermore, the specific surface area of 10RGO/Si-600 (539 m²/g) is further increased after the calcination process, indicating the optimization of the composite structure, which is a critical point for the enhanced cycling stability.

The morphology of the GO, P-Si, and RGO/Si composites were characterized by scanning electron microscopy (SEM). As shown in Figure 4c, 10RGO/Si showed the typical composite structure, indicating that the pure silicon nanoparticles were attached on the surface of graphene to further interconnect into the 3D conductive skeleton network. It can be clearly observed that the 10RGO/Si showed the better 3D

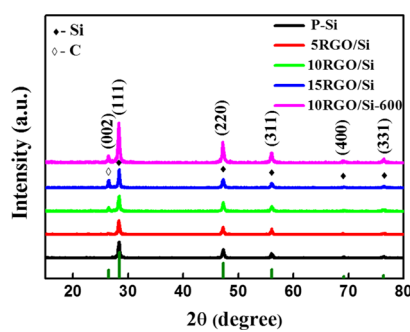


Figure 2. XRD patterns of P-Si and different RGO/Si composites.

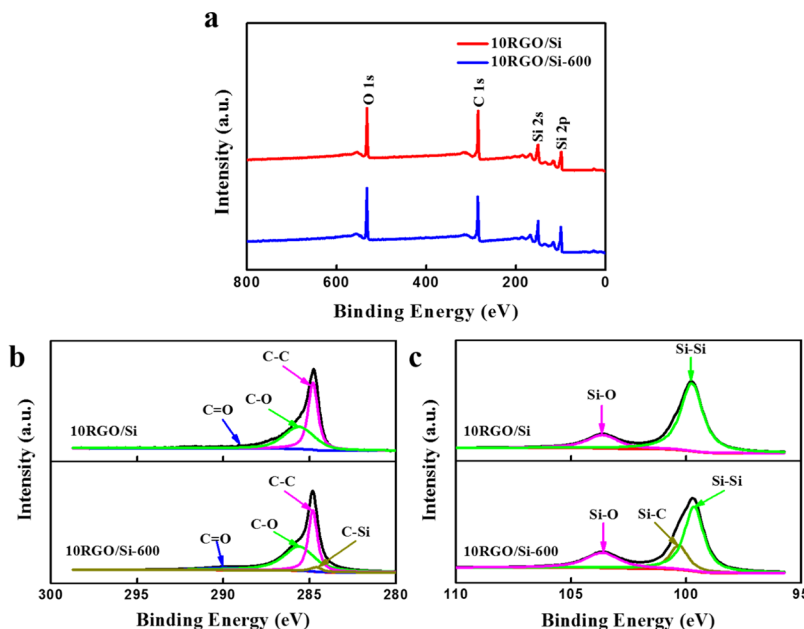


Figure 3. XPS spectra of 10RGO/Si and 10RGO/Si-600: (a) survey scan, (b) region spectra of C 1s, and (c) region spectra of Si 2p.

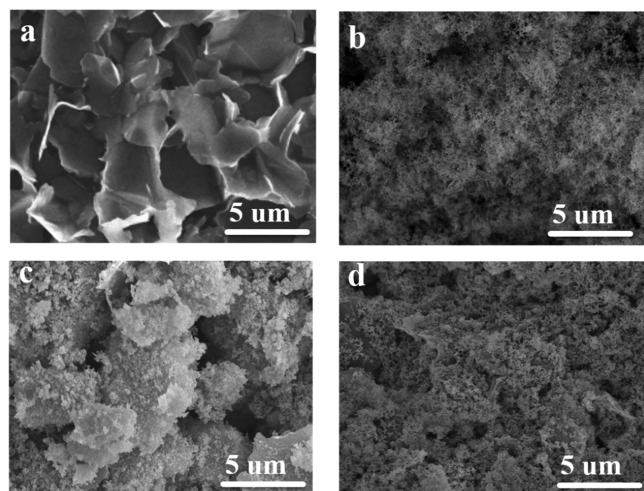


Figure 4. SEM images of (a) graphene oxide; (b) P-Si; (c) 10RGO/Si, and (d) 10RGO/Si-600.

network with the uniformly distributed Si nanoparticles than SRGO/Si and 15RGO/Si (Figure S3a,b). After high-temperature calcination at 600, the 10RGO/Si-600 composite presented a more dense structure, which is beneficial to optimize the transport path for both electrons and electrolyte ions and keep good electrical contact during Si alloying and dealloying process, resulting in an increase of storage capacity and cycling stability.⁴⁰

Transmission electron microscopy (TEM) was further used to analyze the microstructures of P-Si and 10RGO/Si-600. As shown in Figure 5a, P-Si exhibit an average size of about 60 nm with a certain degree of aggregation. From the TEM image of 10RGO/Si-600 (Figure 5b) at the same ruler, Si nanoparticles were supported on the surface of graphene. Furthermore, the high-resolution TEM images (Figure 5c,d) showed that the optimized 10RGO/Si-600 composite can form a 3D network structure, which is consistent with the above SEM images. Also, it can be found that the lattice

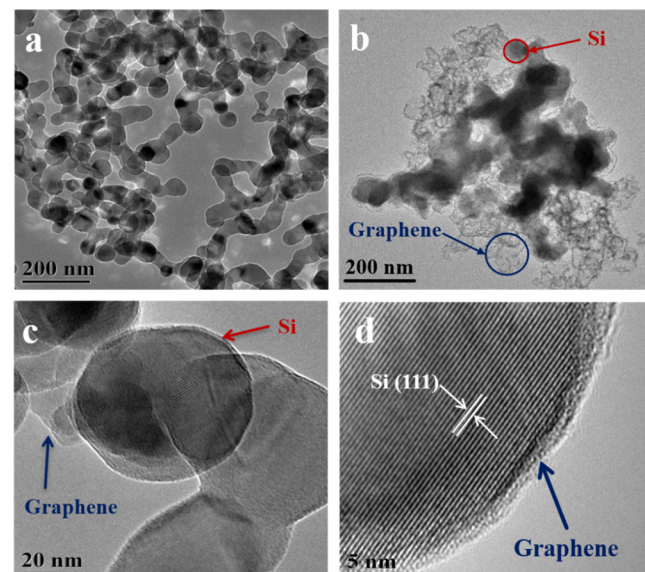


Figure 5. TEM images of (a) pure Si and (b–d) 10RGO/Si-600 composite at different resolutions.

spacing is about 0.32 nm of Si(111) and the microstructure of graphene with high-resolution (Figure S4), which is very important for the improved electrochemical performance due to the large specific surface area based on the BET data. The existence of graphene can accommodate the volume change and enhance the conductivity of lithium ions and electrons. In addition, after high-temperature calcination, the 10RGO/Si-600 composite showed a better crystal structure and a more stable network that can further enhance the composite conductivity and decrease the resistance of Li⁺ transfer. Moreover, the energy dispersive spectrometry (EDS) analysis was utilized to confirm the content (Figure S5) and the distribution of each element in 10RGO/Si-600 (Table S2), which is very much in agreement with the aforementioned analysis.

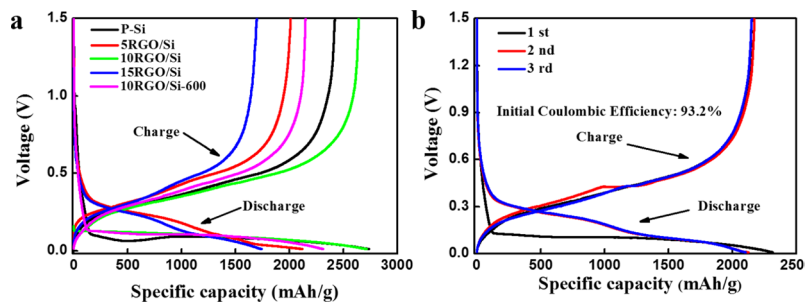


Figure 6. (a) First charge–discharge capacity of different materials and (b) first three charge–discharge curves of 10RGO/Si-600 at 0.1 A/g.

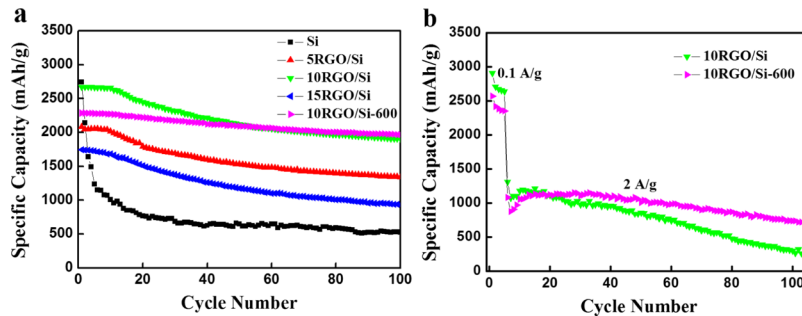


Figure 7. Cycle performance of (a) P-Si and RGO/Si composites under 0.1 A/g and (b) 10RGO/Si and 10RGO/Si-600 under 2 A/g current.

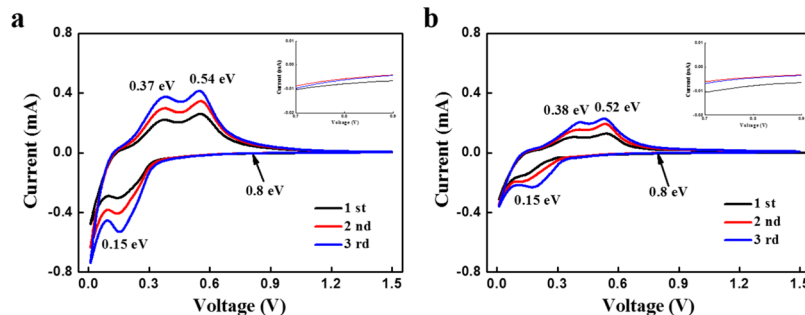


Figure 8. CV curves of (a) 10RGO/Si and (b) 10RGO/Si-600 at the first three cycles with the enlarged view in the inset.

2.2. Evaluation of Electrochemical Performance. The galvanostatic discharge and charge profiles of the RGO/Si electrodes were investigated in the voltage window of 0.01–1.5 V at 0.1 A/g (Figure 6a). Usually, the cycling stability of a Si-based electrode is investigated after the prestabilization process by cycling at a relatively low current density in the range of 0.1–0.4 A/g. It should be mentioned that the cycling stability of the RGO/Si electrode was directly investigated at 0.1 A/g without the preslow cycling process. The corresponding initial charge capacities, discharge capacities, and the coulomb efficiencies are displayed in Figure 6a and summarized in Table S3. As we know, the capacity loss in the first cycle can be attributed to the formation of the solid-electrolyte interphase (SEI) and amorphous Li_xSi.⁴¹ As shown in Figures 6b and S6, the 10RGO/Si-600 and 10RGO/Si electrodes both exhibited excellent cycling stability at the first three cycles and high initial Coulombic efficiency, which is significantly much higher than those of other composites and comparable to the recently reported Si-based electrodes.^{27,32} This is because the formed 3D network played an important role in cycling stability and Coulombic efficiency.⁴²

The cycling performance was also studied by the galvanostatic discharge–charge measurement within 100

cycles under 0.1 and 2 A/g. From Figure 7a, although P-Si has the highest discharge capacity of 2746 mA h/g under 0.1 A/g, the specific capacity of P-Si rapidly decays to 500 mA h/g after 30 cycles due to the huge volume change and the low electronic conductivity during lithiation/delithiation. We can find that all RGO/Si composites showed a better cycle performance than P-Si. Among these, 10RGO/Si-600 showed the high initial discharge capacity of 2317 mA h/g and high capacity retention of 85% after 100 cycles, indicating a quite high specific capacity of 1969 mA h/g attributed to the stable 3D network. Also, from Figure 7b, 10RGO/Si-600 exhibited a better cycling stability than 10RGO/Si after 100 cycles at 2 A/g. Meanwhile, 10RGO/Si-600 showed a higher specific capacity of 728 mA h/g than 10RGO/Si of only 285 mA h/g. Based on the summary and comparison of the recent GO/Si anode (Table S5), the 10RGO/Si-600 composite showed a much higher specific capacity after 100 cycles at 0.1 A/g and is comparable to the best anode materials after 100 cycles at 2 A/g. It is because the optimized 3D network leads to an increase in the specific surface area and intermolecular interaction, which is very important for electrochemical performance.^{43,44} This kind of optimized graphene/Si nanocomposite holds great promise for the future LIB application.

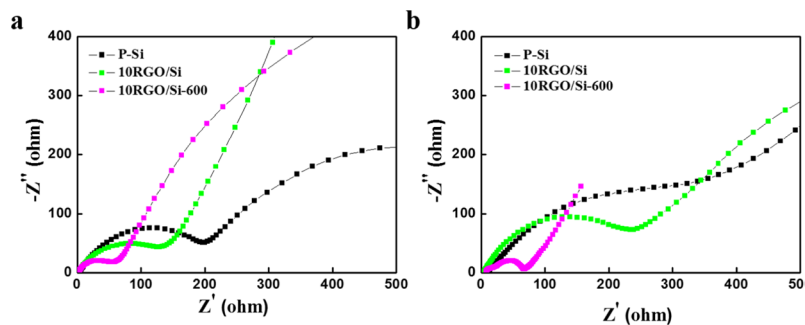


Figure 9. EIS of P–Si, 10RGO/Si, and 10RGO/Si-600 electrodes (a) before and (b) after 100 cycles.

Furthermore, the 10RGO/Si-600 electrode also shows an excellent rate capability (Figure S7 and Table S4), as estimated by varying the applied current densities of 0.1, 0.3, 0.5, and 1 A/g, respectively. When the current density is increased from 0.1 to 1 A/g, 70% of the initial reversible capacity (~1730 mA h/g) is maintained. Even though the 10RGO/Si-600 electrode reversible capacity is recovered to about 2156 mA h/g and the capacity retention ratio is about 88%, when the current density is back to 0.1 A/g after 25 cycles.

Figure 8 shows the first three cyclic voltammetry (CV) curves of P–Si, 10RGO/Si, and 10RGO/Si-600 electrodes at a scanning rate of 0.1 mV/s with a voltage range of 0.01–1.5 V (vs Li/Li⁺). As shown in Figure S8, the typical lithiation/delithiation peaks of Si nanoparticles were exhibited in their CV curves. During the first discharge (lithiation), two cathodic peaks can be observed. One peak is around 0.8 V due to the formation of an SEI layer, which disappears in the following cycles, indicating that the SEI layer is stable. Another peak below 0.15 V is assigned to the preliminary conversion of crystalline Si transfer to an amorphous phase (Li_xSi) and the ultimate formation of the crystalline phase (Li₁₅Si₄). For the first charge process (delithiation), two anodic peaks at 0.37 and 0.54 V are corresponding to the transformation from Li₁₅Si₄ alloy to amorphous Si. With the subsequent cycling, the cathodic peak moves to about 0.1 V, indicating that only the amorphous phase (Li_xSi) is formed, and two anodic peaks (0.37 and 0.54 V) represent the extraction of Li⁺ from Li_xSi to amorphous Si.^{45–47} Both the 10RGO/Si and 10RGO/Si-600 electrodes exhibit similar CV behavior. For the 10RGO/Si-600 composite, the second CV curve of the 10RGO/Si-600 electrode almost coincides with the third curve, and the decrease of the peak current below 0.1 mA in the cathodic curves is much less than that for the 10RGO/Si electrode, indicating that the stability and good reversibility of the charging/discharging of the 10RGO/Si-600 (Figure 8a) electrode is better than that for the 10RGO/Si (Figure 8b) electrode.

The electrochemical impedance spectroscopy (EIS) experiments of P–Si, 10RGO/Si, and 10RGO/Si-600 were carried out to further discuss the electrical conductivity performance (Figure 9a). All Nyquist plots show similar shape with a semicircle in the high-frequency region and a straight line in the low-frequency region. The semicircle in the high-frequency region is assigned to the transportation barrier effect as a result of the confronted SEI and shows the presence of graphene, and a straight-line in the range from the medium to low frequency is a result of the diffusive behavior of Li⁺ ions. These resistances included the resistance of ion transportation within the electrolyte solution (R_{e}) and the charge-transfer resistance

(R_{ct}).⁴⁸ As we all know, the charge-transfer resistance of 10RGO/Si-600 electrode is 53.1 Ω, which is slower than the 124.2 Ω of the 10RGO/Si and 196 Ω of the P–Si, indicating the higher electrochemical activity of 10RGO/Si-600 than that of other composites after 100 cycles (Figure 9b), which is consistent with the result of the cycling test.

The microstructures of P–Si, 10RGO/Si, and 10RGO/Si-600 electrodes were characterized by SEM after 100 cycles (Figure 10). Obviously, the microstructure of P–Si has been

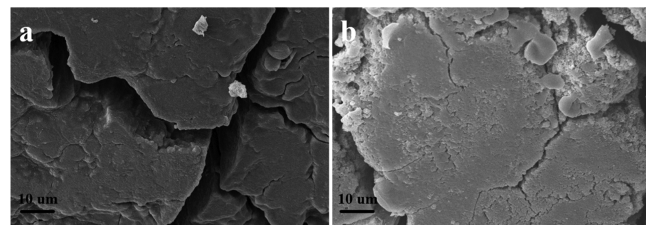


Figure 10. SEM images of the (a) 10RGO/Si and (b) 10RGO/Si-600 electrodes after 100 charge/discharge cycles at 0.1 A/g.

severely damaged and pulverized, whereas the 10RGO/Si and 10RGO/Si-600 electrodes showed better surface structure after 100 cycles. Especially, the microstructure of 10RGO/Si-600 was more integrated than 10RGO/Si due to the enhanced intermolecular interaction between graphene and Si nanoparticles after the calcination process, resulting in an increase of cycling stability.

3. CONCLUSIONS

The optimized RGO/Si composite has been successfully prepared by an effective method for high-performance LIB application. TEM and EDS measurements showed that the silicon nanoparticles were uniformly distributed on the surface of RGO, which can form a 3D network resulting in an increase of the electronic conductivity and structural stability for the anode material. The 10RGO/Si-600 composite shows excellent initial specific capacity of 2317 mA h/g with initial Coulombic efficiency of about 93.2% at a current density of 0.1 A/g. The specific capacity remains at 728 mA h/g after 100 cycles at 2 A/g, indicating a high rate cycle stability. The remarkable electrochemical performance can be attributed to the stable 3D structure, which can effectively improve the electroperformance and buffer the volume expansion during the cycling process. This work opens up a new method for making advanced graphene/Si nanocomposites for high stability LIBs.

4. EXPERIMENTAL SECTION

4.1. Sample Preparation. All reagents, unless otherwise stated, were obtained from commercial sources (Sigma-Aldrich) and used without further purification. Graphene oxide was synthesized by the modified Hummers method.⁴⁹ The preparation process of the optimized RGO/Si nanocomposite is as follows. First, the as-prepared graphene oxide (0.05, 0.1, 0.15 g) was dispersed in 50 mL of absolute ethanol under high-power ultrasonic stirring technology for 1 h at room temperature. Then, the preprocessed silicon (0.95, 0.90, 0.85 g) was slowly added into the above solution under magnetic stirring. After that, the self-assembled RGO/Si solution was acquired by mild stirring for 2 h and dialysis in absolute ethanol several times (12 h per time) at room temperature to remove the unassembled Si particles.^{50,51} Then, the self-assembled solution was transferred to the reaction still for hydrothermal reduction for 3 h at 80 °C by a certain amount of sodium borohydride to obtain RGO/Si. In the experiment, the different quality ratios of the RGO/Si samples were denoted as x RGO/Si ($x = 5, 10, 15$). In addition, the 10RGO/Si composite was calcined at 600 °C for 4 h with argon atmosphere in a tube furnace to further optimize the nanostructure and enhance the interactions, which was marked as 10RGO/Si-600. Finally, the optimized RGO/Si composites as the working electrode were assembled into half coin cell. In contrast, the unmodified silicon was marked as P-Si. The whole preparation process of the optimized RGO/Si composite can be defined as the templated assembly method, which can be applied for similar nanotemplated platform and Si composite.

4.2. Materials Characterization. X-ray diffraction (D/MAX-Ultima IV, Japan) was carried out with Cu K α radiation in the 2θ range from 10° to 80°. The particle morphology and microstructure were characterized by field emission SEM (S-3400, Japan), TEM (FEI Tecnai G2 F20 s-twin 200 kV) with an energy dispersive spectroscopy (EDS) analyzer. The chemical oxidation valence states of the samples were performed through X-ray photoelectron spectroscopy (XPS, Thermo Scientific ESCALAB 250Xi). The BET (3H-2000PS1, Beishide Instrument) test was applied for the specific surface area.

4.3. Electrochemical Analysis. The prepared RGO/Si composite materials were mixed with carbon black and a binder (sodium carboxymethyl cellulose) with a mass ratio of 70:15:15 for several hours. Then, the slurry was coated on a copper foil at a mass loading of around 1.5 mg/cm². The prepared electrodes were vacuum dried at 80 °C for 10 h. Finally, the electrodes were cut into disk shape; a CR2032 cell was assembled in an argon-filled glove box, taking lithium metal as the counter and reference electrodes and microporous polypropylene (Celgard 2400) as the separator. The electrolyte of half cells was 1 M LiPF₆ in a mixture of ethylene carbonate/dimethyl carbonate with a volume ratio of 1:1, and adding 5% fluoroethylene carbonate. Half coin-cells were assembled in an Ar-filled glove box with the moisture and oxygen level below 0.1 ppm and then rested for 24 h. The galvanostatic charge-discharge tests were measured on a battery testing system (Neware, BTS7.5, China) at room temperature (25 °C ± 1 °C) under a voltage range of 0.01–1.5 V versus Li/Li⁺. CV measurements were carried out on an electrochemical workstation (CHI670D, CH Instruments) at a scanning rate of 0.1 mV/s in a voltage range of 0.01–1.5 V. The EIS

measurements were also conducted by electrochemical workstation CHI670D with an amplitude of 5 mV at the frequency range from 0.01 Hz to 100 kHz.

■ ASSOCIATED CONTENT

■ Supporting Information

The Supporting Information is available free of charge on the ACS Publications website at DOI: [10.1021/acsomega.9b02089](https://doi.org/10.1021/acsomega.9b02089).

XPS spectra of P-Si; adsorption/desorption of 10RGO/Si-600; SEM images of 5RGO/Si and 15RGO/Si; TEM image of graphene nanosheet; EDS of the 10RGO/Si-600 composite; first charge-discharge capacity of 10RGO/Si at 0.1 A/g; rate performance of P-Si and RGO/Si composites at various current densities; CV curves of P-Si electrode at the first three cycles; SEM images of the P-Si after 100 charge/discharge cycles; BET data; ; EDS analysis of each element; initial charge-discharge capacities and corresponding coulombic efficiency of the P-Si and RGO/Si; cycle performance of P-Si and RGO/Si at different current; electrochemical performance of 10RGO/Si-600 ([PDF](#))

■ AUTHOR INFORMATION

Corresponding Authors

*E-mail: pklxx@gdut.edu.cn (X.L.).

*E-mail: wenluo@gdut.edu.cn (W.L.).

ORCID

Xinxi Li: [0000-0001-5014-1678](https://orcid.org/0000-0001-5014-1678)

Author Contributions

§X.L. and W.L. contributed equally to this work.

Notes

The authors declare no competing financial interest.

■ ACKNOWLEDGMENTS

This work was supported by the National Natural Science Foundation of China (grant no. 21875046, no. 51803036, and no. 51876044), Technology Plan Scientific Research Project of Guangzhou city (no. 201607010259), and Science and Technology Innovation Project of Foshan city (no. 2017IT100143).

■ REFERENCES

- (1) Zhang, X.; Qiu, X.; Kong, D.; Zhou, L.; Li, Z.; Li, X.; Zhi, L. Silicene Flowers: A Dual Stabilized Silicon Building Block for High-Performance Lithium Battery Anodes. *ACS Nano* **2017**, *11*, 7476–7484.
- (2) Choi, M.; Kim, J. C.; Kim, D. W. Waste Windshield-Derived Silicon/Carbon Nanocomposites as High-Performance Lithium-Ion Battery Anodes. *Sci. Rep.* **2018**, *8*, 960.
- (3) Ma, X.; Gao, Y.; Chen, M.; Wu, L. Synthesis of Robust Silicon Nanoparticles@Void@Graphitic Carbon Spheres for High-Performance Lithium-Ion-Battery Anodes. *ChemElectroChem* **2017**, *4*, 1463–1469.
- (4) Jansen, A. N.; Kahaian, A. J.; Kepler, K. D.; Nelson, P. A.; Amine, K.; Dees, D. W.; Vissers, D. R.; Thackeray, M. M. Development of a High-Power Lithium-Ion Battery. *J. Power Sources* **1999**, *81–82*, 902–905.
- (5) Casimir, A.; Zhang, H.; Ogoke, O.; Amine, J. C.; Lu, J.; Wu, G. Silicon-Based Anodes for Lithium-Ion Batteries: Effectiveness of Materials Synthesis and Electrode Preparation. *Nano Energy* **2016**, *27*, 359–376.

- (6) Park, J. H.; Moon, J.; Han, S.; Park, S.; Lim, J. W.; Yun, D.-J.; Kim, D. Y.; Park, K.; Son, I. H. Formation of Stable Solid-Electrolyte Interphase Layer on Few-Layer Graphene-Coated Silicon Nanoparticles for High-Capacity Li-ion Battery Anodes. *J. Phys. Chem. C* **2017**, *121*, 26155–26162.
- (7) Chen, Y.; Hu, Y.; Shen, Z.; Chen, R.; He, X.; Zhang, X.; Zhang, Y.; Wu, K. Sandwich Structure of Graphene-Protected Silicon/Carbon Nanofibers for Lithium-Ion Battery Anodes. *Electrochim. Acta* **2016**, *210*, 53–60.
- (8) Ye, Q.; Zheng, P.; Ao, X.; Yao, D.; Lei, Z.; Deng, Y.; Wang, C. Novel Multi-Block Conductive Binder with Polybutadiene for Si Anodes in Lithium-Ion Batteries. *Electrochim. Acta* **2019**, *315*, 58–66.
- (9) Kovalenko, I.; Zdyrko, B.; Magasinski, A.; Hertzberg, B.; Milicev, Z.; Burtovyy, R.; Luzinov, I.; Yushin, G. A Major Constituent of Brown Algae for Use in High-Capacity Li-ion Batteries. *Science* **2011**, *334*, 75–79.
- (10) Choi, S.; Kwon, T.-w.; Coskun, A.; Choi, J. W. Highly Elastic Binders Integrating Polyrotaxanes for Silicon Microparticle Anodes in Lithium-Ion Batteries. *Science* **2017**, *357*, 279–283.
- (11) Wang, C.; Wu, H.; Chen, Z.; McDowell, M. T.; Cui, Y.; Bao, Z. Self-Healing Chemistry Enables the Stable Operation of Silicon Microparticle Anodes for High-Energy Lithium-Ion Batteries. *Nat. Chem.* **2013**, *5*, 1042–1048.
- (12) Dalavi, S.; Guduru, P.; Lucht, B. L. Performance Enhancing Electrolyte Additives for Lithium-Ion Batteries with Silicon Anodes. *J. Electrochem. Soc.* **2012**, *159*, A642–A646.
- (13) Xu, C.; Lindgren, F.; Philippe, B.; Gorgoi, M.; Björrefors, F.; Edström, K.; Gustafsson, T. Improved Performance of Silicon Anode for Li-ion Batteries: Understanding the Surface Modification Mechanism of Fluoroethylene Carbonate as an Effective Electrolyte Additive. *Chem. Mater.* **2015**, *27*, 2591–2599.
- (14) Chen, X.; Li, X.; Mei, D.; Feng, J.; Hu, M. Y.; Hu, J.; Engelhard, M.; Zheng, J.; Xu, W.; Xiao, J.; Liu, J.; Zhang, J.-G. Reduction Mechanism of Fluoroethylene Carbonate for Stable Solid-Electrolyte Interphase Film on Silicon Anode. *ChemSusChem* **2014**, *7*, 549–554.
- (15) Jin, Y.; Li, S.; Kushima, A.; Zheng, X. Q.; Sun, Y. M.; Xie, J.; Sun, J.; Xue, W. J.; Zhou, G. M.; Wu, J.; Shi, F. F.; Zhang, R. F.; Zhu, Z.; So, K. P.; Cui, Y.; Li, J. Self-Healing SEI Enables Full-Cell Cycling of a Silicon-Majority Anode with a Coulombic Efficiency Exceeding 99.9%. *Energy Environ. Sci.* **2017**, *10*, 580–592.
- (16) An, W.; Fu, J.; Su, J.; Wang, L.; Peng, X.; Wu, K.; Chen, Q.; Bi, Y.; Gao, B.; Zhang, X. Mesoporous Hollow Nanospheres Consisting of Carbon Coated Silica Nanoparticles for Robust Lithium-Ion Battery Anodes. *J. Power Sources* **2017**, *345*, 227–236.
- (17) Li, X.; Yan, P.; Arey, B. W.; Luo, W.; Ji, X.; Wang, C.; Liu, J.; Zhang, J.-G. A Stable Nanoporous Silicon Anode Prepared by Modified Magnesiothermic Reactions. *Nano Energy* **2016**, *20*, 68–75.
- (18) Li, X.; Gu, M.; Hu, S. Y.; Kennard, R.; Yan, P. F.; Chen, X. L.; Wang, C. M.; Sailor, M. J.; Zhang, J. G.; Liu, J. Mesoporous Silicon Sponge as an Anti-Pulverization Structure for High-Performance Lithium-Ion Battery Anodes. *Nat. Commun.* **2014**, *5*, 4105.
- (19) An, W. L.; Gao, B.; Mei, S. X.; Xiang, B.; Fu, J. J.; Wang, L.; Zhang, Q. B.; Chu, P. K.; Huo, K. F. Scalable Synthesis of Ant-Nest-Like Bulk Porous Silicon for High-Performance Lithium-Ion Battery Anodes. *Nat. Commun.* **2019**, *10*, 1447.
- (20) Wang, W.; Kumta, P. N. Nanostructured Hybrid Silicon/Carbon Nanotube Heterostructures: Reversible High-Capacity Lithium-Ion Anodes. *ACS Nano* **2010**, *4*, 2233–2241.
- (21) Ryou, M.-H.; Kim, J.; Lee, I.; Kim, S.; Jeong, Y. K.; Hong, S.; Ryu, J. H.; Kim, T.-S.; Park, J.-K.; Lee, H.; Choi, J. W. Mussel-Inspired Adhesive Binders for High-Performance Silicon Nanoparticle Anodes in Lithium-Ion Batteries. *Adv. Mater.* **2013**, *25*, 1570.
- (22) Roginskaya, Y. E.; Kulova, T. L.; Skundin, A. M.; Bruk, M. A.; Zhikharev, E. N.; Kal'nov, V. A. Lithium Insertion into Silicon Films Produced by Magnetron Sputtering. *Russ. J. Electrochem.* **2008**, *44*, 992–1001.
- (23) Zhang, X.-W.; Patil, P. K.; Wang, C.; Appleby, A. J.; Little, F. E.; Cocke, D. L. Electrochemical Performance of Lithium-Ion Battery, Nano-Silicon-Based, Disordered Carbon Composite Anodes with Different Microstructures. *J. Power Sources* **2004**, *125*, 206–213.
- (24) Wang, B.; Li, X.; Zhang, X.; Luo, B.; Jin, M.; Liang, M.; Dayeh, S. A.; Picraux, S. T.; Zhi, L. Adaptable Silicon-Carbon Nanocables Sandwiched between Reduced Graphene Oxide Sheets as Lithium Ion Battery Anodes. *ACS Nano* **2013**, *7*, 1437–1445.
- (25) An, W.; Xiang, B.; Fu, J.; Mei, S.; Guo, S.; Huo, K.; Zhang, X.; Gao, B.; Chu, P. K. Three-Dimensional Carbon-Coating Silicon Nanoparticles Welded on Carbon Nanotubes Composites for High-Stability Lithium-Ion Battery Anodes. *Appl. Surf. Sci.* **2019**, *479*, 896–902.
- (26) An, W.; Fu, J.; Mei, S.; Xia, L.; Li, X.; Gu, H.; Zhang, X.; Gao, B.; Chu, P. K.; Huo, K. Dual Carbon Layer Hybridized Mesoporous Tin Hollow Spheres for Fast-Rechargeable and Highly-Stable Lithium-Ion Battery Anodes. *J. Mater. Chem. A* **2017**, *5*, 14422–14429.
- (27) Chou, S.-L.; Wang, J.-Z.; Choucair, M.; Liu, H.-K.; Stride, J. A.; Dou, S.-X. Enhanced Reversible Lithium Storage in a Nanosize Silicon/Graphene Composite. *Electrochem. Commun.* **2010**, *12*, 303–306.
- (28) Chang, J.; Huang, X.; Zhou, G.; Cui, S.; Hallac, P. B.; Jiang, J.; Hurley, P. T.; Chen, J. Multilayered Si Nanoparticle/Reduced Graphene Oxide Hybrid as a High-Performance Lithium-Ion Battery Anode. *Adv. Mater.* **2014**, *26*, 758–764.
- (29) Park, S.-H.; Kim, H.-K.; Ahn, D.-J.; Lee, S.-I.; Roh, K. C.; Kim, K.-B. Self-Assembly of Si Entrapped Graphene Architecture for High-Performance Li-ion Batteries. *Electrochem. Commun.* **2013**, *34*, 117–120.
- (30) Son, I. H.; Park, J. H.; Kwon, S.; Park, S.; Rummeli, M. H.; Bachmatiuk, A.; Song, H. J.; Ku, J.; Choi, J. W.; Choi, J. M.; Doo, S. G.; Chang, H. Silicon Carbide-Free Graphene Growth on Silicon for Lithium-Ion Battery with High Volumetric Energy Density. *Nat. Commun.* **2015**, *6*, 7393.
- (31) Zhou, M.; Li, X.; Wang, B.; Zhang, Y.; Ning, J.; Xiao, Z.; Zhang, X.; Chang, Y.; Zhi, L. High-Performance Silicon Battery Anodes Enabled by Engineering Graphene Assemblies. *Nano Lett.* **2015**, *15*, 6222–6228.
- (32) Zhang, K.; Xia, Y.; Yang, Z.; Fu, R.; Shen, C.; Liu, Z. Structure-Preserved 3D Porous Silicon/Reduced Graphene Oxide Materials as Anodes for Li-ion Batteries. *RSC Adv.* **2017**, *7*, 24305–24311.
- (33) Zhang, R.; Du, Y.; Li, D.; Shen, D.; Yang, J.; Guo, Z.; Liu, H. K.; Elzatahry, A. A.; Zhao, D. Highly Reversible and Large Lithium Storage in Mesoporous Si/C Nanocomposite Anodes with Silicon Nanoparticles Embedded in a Carbon Framework. *Adv. Mater.* **2014**, *26*, 6749–6755.
- (34) He, Z.; Wu, X.; Yi, Z.; Wang, X.; Xiang, Y. Silicon/Graphene/Carbon Hierarchical Structure Nanofibers for High Performance Lithium Ion Batteries. *Mater. Lett.* **2017**, *200*, 128–131.
- (35) Huang, Y.; Wu, D.; Jiang, J.; Mai, Y.; Zhang, F.; Pan, H.; Feng, X. Highly Oriented Macroporous Graphene Hybrid Monoliths for Lithium Ion Battery Electrodes with Ultrahigh Capacity and Rate Capability. *Nano Energy* **2015**, *12*, 287–295.
- (36) Zhao, Q.; Huang, Y.; Hu, X. A Si/C Nanocomposite Anode by Ball Milling for Highly Reversible Sodium Storage. *Electrochem. Commun.* **2016**, *70*, 8–12.
- (37) Chang, P.; Liu, X.; Zhao, Q.; Huang, Y.; Huang, Y.; Hu, X. Constructing Three-Dimensional Honeycombed Graphene/Silicon Skeletons for High-Performance Li-ion Batteries. *ACS Appl. Mater. Interfaces* **2017**, *9*, 31879–31886.
- (38) Fang, M.; Wang, Z.; Chen, X.; Guan, S. Sponge-Like Reduced Graphene Oxide/Silicon/Carbon Nanotube Composites for Lithium Ion Batteries. *Appl. Surf. Sci.* **2018**, *436*, 345–353.
- (39) Wang, M.-S.; Wang, Z.-Q.; Jia, R.; Yang, Y.; Zhu, F.-Y.; Yang, Z.-L.; Huang, Y.; Li, X.; Xu, W. Facile Electrostatic Self-Assembly of Silicon/Reduced Graphene Oxide Porous Composite by Silica Assist as High Performance Anode for Li-ion Battery. *Appl. Surf. Sci.* **2018**, *456*, 379–389.
- (40) Yue, H.; Li, Q.; Liu, D.; Hou, X.; Bai, S.; Lin, S.; He, D. High-Yield Fabrication of Graphene-Wrapped Silicon Nanoparticles for

Self-Support and Binder-Free Anodes of Lithium-Ion Batteries. *J. Alloys Compd.* **2018**, *744*, 243–251.

(41) Chen, Y.; Li, Y.; Wang, Y.; Fu, K.; Danner, V. A.; Dai, J.; Lacey, S. D.; Yao, Y.; Hu, L. Rapid, *in Situ* Synthesis of High Capacity Battery Anodes through High Temperature Radiation-Based Thermal Shock. *Nano Lett.* **2016**, *16*, 5553–5558.

(42) Liu, X.; Zhang, J.; Si, W.; Xi, L.; Eichler, B.; Yan, C.; Schmidt, O. G. Sandwich Nano Architecture of Si/Reduced Graphene Oxide Bilayer Nanomembranes for Li-ion Batteries with Long Cycle Life. *ACS Nano* **2015**, *9*, 1198–1205.

(43) Sun, W.; Hu, R.; Liu, H.; Zeng, M.; Yang, L.; Wang, H.; Zhu, M. Embedding Nano-Silicon in Graphene Nanosheets by Plasma Assisted Milling for High Capacity Anode Materials in Lithium-Ion Batteries. *J. Power Sources* **2014**, *268*, 610–618.

(44) Sun, W.; Hu, R.; Zhang, H.; Wang, Y.; Yang, L.; Liu, J.; Zhu, M. A Long-Life Nano-Silicon Anode for Lithium-Ion Batteries: Supporting of Graphene Nanosheets Exfoliated from Expanded Graphite by Plasma-Assisted Milling. *Electrochim. Acta* **2016**, *187*, 1–10.

(45) Yao, M.; Zeng, Z.; Zhang, H.; Yan, J.; Liu, X. Electrophoretic Deposition of Carbon Nanofibers/Silicon Film with Honeycomb Structure As Integrated Anode Electrode for Lithium-Ion Batteries. *Electrochim. Acta* **2018**, *281*, 312–322.

(46) Wu, J.; Qin, X.; Zhang, H.; He, Y.-B.; Li, B.; Ke, L.; Lv, W.; Du, H.; Yang, Q.-H.; Kang, F. Multilayered Silicon Embedded Porous Carbon/Graphene Hybrid Film as A High Performance Anode. *Carbon* **2015**, *84*, 434–443.

(47) Hassan, F. M.; Chabot, V.; Elsayed, A. R.; Xiao, X.; Chen, Z. Engineered Si Electrode Nanoarchitecture: A Scalable Postfabrication Treatment for the Production of Next-Generation Li-ion Batteries. *Nano Lett.* **2014**, *14*, 277–283.

(48) Tao, H.; Xiong, L.; Zhu, S.; Zhang, L.; Yang, X. Porous Si/C/ Reduced Graphene Oxide Microspheres by Spray Drying as Anode for Li-ion Batteries. *J. Electroanal. Chem.* **2017**, *797*, 16–22.

(49) Park, S.; An, J.; Potts, J. R.; Velamakanni, A.; Murali, S.; Ruoff, R. S. Hydrazine-Reduction of Graphite- and Graphene Oxide. *Carbon* **2011**, *49*, 3019–3023.

(50) Luo, W.; Feng, Y.; Cao, C.; Li, M.; Liu, E.; Li, S.; Qin, C.; Hu, W.; Feng, W. A high energy density azobenzene/graphene hybrid: a nano-templated platform for solar thermal storage. *J. Mater. Chem. A* **2015**, *3*, 11787–11795.

(51) Kucharski, T. J.; Ferralis, N.; Kolpak, A. M.; Zheng, J. O.; Nocera, D. G.; Grossman, J. C. Templated assembly of photoswitches significantly increases the energy-storage capacity of solar thermal fuels. *Nat. Chem.* **2014**, *6*, 441.